SANDIA REPORT
SAND2021-15041
Printed Click to enter a date

Sandia National Laboratories

Quantitative assessment of Distributed Acoustic Sensing at the Source Physics Experiment, Phase II

Robert W. Porritt
Robert E. Abbott
Christian Poppeliers

Prepared by Robert W. Porritt
Sandia National Laboratories
Albuquerque, New Mexico
87185 and Livermore,
California 94550

Issued by Sandia National Laboratories, operated for the United States Department of Energy by National Technology & Engineering Solutions of Sandia, LLC.

Available to DOE and DOE contractors from
U.S. Department of Energy
Office of Scientific and Technical Information
P.O. Box 62
Oak Ridge, TN 37831

Telephone: (865) 576-8401
Facsimile: (865) 576-5728
E-Mail: reports@osti.gov
Online ordering: http://www.osti.gov/scitech

Available to the public from
U.S. Department of Commerce
National Technical Information Service
5301 Shawnee Rd
Alexandria, VA 22312

Telephone: (800) 553-6847
Facsimile: (703) 605-6900
E-Mail: orders@ntis.gov
Online order: https://classic.ntis.gov/help/order-methods/

ABSTRACT

In this report, we assess the data recorded by a Distributed Acoustic Sensing (DAS) cable deployed during the Source Physics Experiment, Phase II (DAG) in comparison with the data recorded by nearby 4.5-Hz geophones. DAS is a novel recording method with unprecedented spatial resolution, but there are significant concerns around the data fidelity as the technology is ramped up to more common usage. Here we run a series of tests to quantify the similarity between DAS data and more conventional data and investigate cases where the higher spatial resolution of the DAS can provide new insights into the wavefield. These tests include 1D modeling with seismic refraction and bootstrap uncertainties, assessing the amplitude spectra with distance from the source, measuring the frequency dependent inter-station coherency, estimating time-dependent phase velocity with beamforming and semblance, and measuring the cross-correlation between the geophone and the particle velocity inferred from the DAS. In most cases, we find high similarity between the two datasets, but the higher spatial resolution of the DAS provides increased details and methods of estimating uncertainty.

ACKNOWLEDGEMENTS

The Source Physics Experiment (SPE) would not have been possible without the support of many people from several organizations. The authors wish to express their gratitude to the National Nuclear Security Administration, Defense Nuclear Nonproliferation Research and Development (DNN R&D), and the SPE working group, a multi-institutional and interdisciplinary group of scientists and engineers

CONTENTS

LIST OF FIGURES

LIST OF TABLES

This page left blank

ACRONYMS AND DEFINITIONS

Abbreviation	Definition
SPE	Source Physics Experiment
DAG	Dry Alluvium Geology
DAG-2	Second explosion of the DAG experiment
DAS	Distributed Acoustic Sensing
P	Compressional
AZ	Arizona
CA	California
NV	Nevada
1D	One-Dimensional
2D	Two-Dimensional
TNT	Trinitrotoluene
Hz	Hertz
m	Meters
kg	Kilogram
m/s	Meters per second
CWT	Continuous Wavelet Transform
PDFs	Probability Density Function
Coh	Coherency
Sem	Semblance
s/km	Seconds per kilometer
SGZ	Surface Ground Zero above the DAG-2 Explosion

1. INTRODUCTION

The Source Physics Experiment (SPE) is a large, multi-year, multi-agency effort to characterize the geophysical phenomena associated with large underground chemical explosions. To accomplish this task, the experiment is distributed amongst three phases designed to isolate the effects of variations in the host medium, variations in the explosive yield, and provide a direct comparison with historical seismicity. In each phase, a series of underground chemical explosions were well recorded by, among other things, a large-N array of 4.5-Hz geophones within ~2 km of the source and broadband seismometers at regional scale distances. In this report, we assess data recorded at the second phase of the experiment. The site of this phase was chosen because the medium is composed of a Dry Alluvium Geology (DAG). In this second phase of the experiment, herein referred to as DAG, the explosion-induced seismic wavefields were recorded by a large array (N = 482) of 4.5-Hz geophones as well as a Distributed Acoustic Sensing (DAS) system in a fiber-optic cable deployed on the surface from 20 meters from the source borehole to ~2 km horizontal distance.

The DAG phase of the experiment (i.e., SPE Phase II, Figure 1-1) provides a significant contrast to the first phase of the experiments in the form of the propagation medium. In SPE Phase I, the explosions were detonated in a granite. There was a significant structural boundary to the northwest of the source point, separating the granite, with a compressional (P) wavespeed of ~3000 m/s, from unconsolidated alluvial materials (e.g. Darrh et al., 2019). For DAG, the explosions were detonated in the dry alluvium filled basin of Yucca Flat (Figure 1-1). These different geologic settings result in markedly different wave propagation effects, such as variations in scattering, explosion containment, and attenuation. In particular, the unconsolidated shallow layer at DAG has a low P wavespeed of ~1500 m/s (Toney et al., 2019) and significant scattering with a mean free path of ~500-580 m (Darrh et. al., in preparation). Underlying the shallow layers is a Tertiary volcanic layer and Paleozoic bedrock which have significantly higher P wavespeeds of ~5000-6000 m/s (e.g. Toney et al., 2019). For clarity, we differentiate between "phase velocity", "wavespeed", and "particle velocity". Phase velocity indicates a vector magnitude and direction of a specific seismic phase propagating through a medium. It is therefore a property of the seismic wavefield. Wavespeed is the magnitude of the phase velocity and is a property of the propagation medium. Particle velocity is the ground motion, typically measured by the geophones.

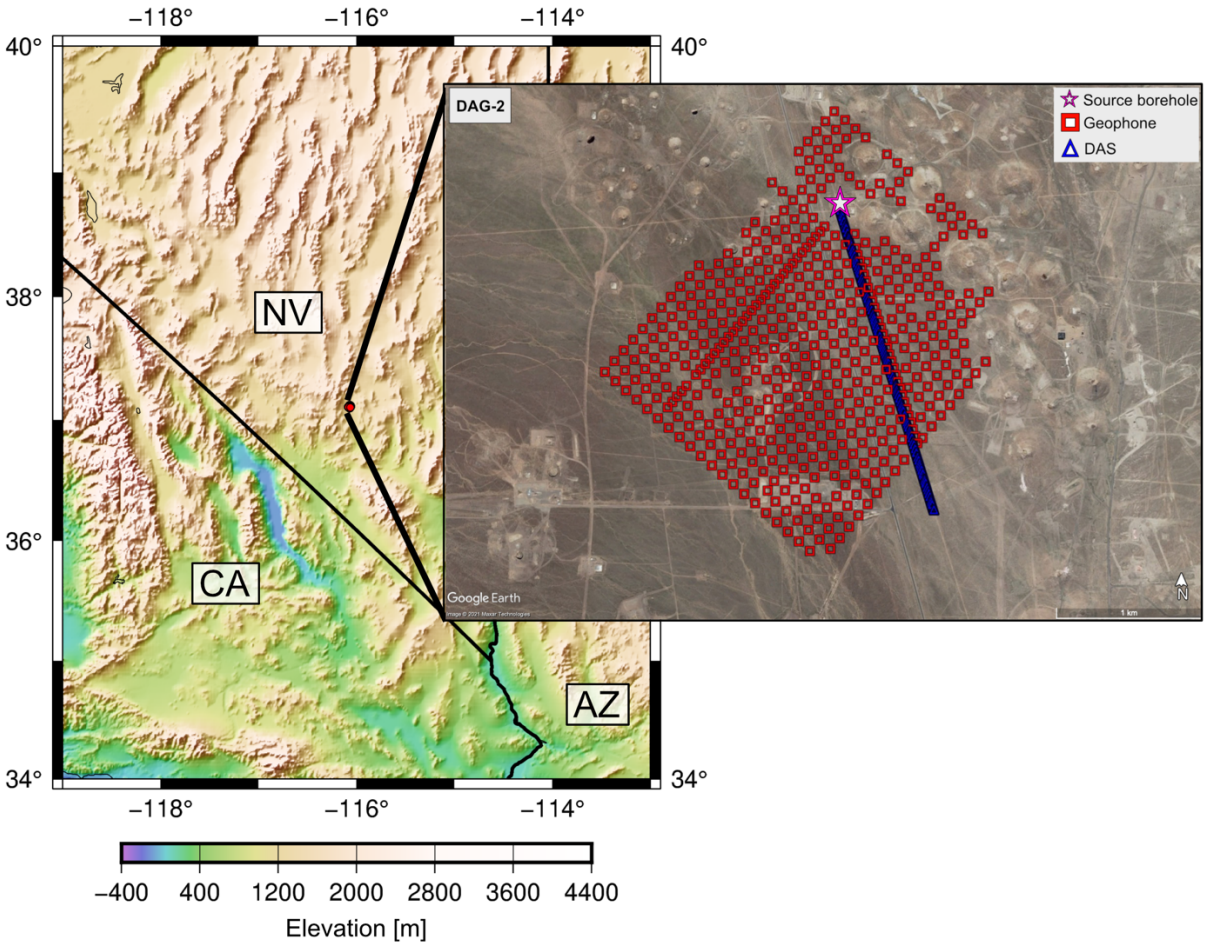

Figure 1-1: Location map of the Dry Alluvium Geology (DAG) source borehole and large-N recording network. State boundaries of Arizona (AZ), California (CA), and Nevada (NV) indicated as black lines. The blue line in the inset indicates the Distributed Acoustic Sensing (DAS) line and spans ~2 km. Aside from the dense lines oriented to the southwest and southeast, geophones are nominally spaced at 50 m inter-station spacing.

An emerging technology in seismic recording is the use of DAS to sample the wavefield at high spatial and temporal resolution (e.g. Zhan, 2020). The technology underlying this method is the use of imperfections in a fiber-optic cable which lead to scattering of light as it passes through the cable. The scattering is proportional to strain-rate along the cable and therefore if the cable is well-coupled to the ground, DAS provides a direct estimate of ground deformation. This is operationally implemented by attaching an interrogator to a fiber-optic cable and having the interrogator send a pulsed light signal down the cable. The interrogator measures the phase-shift in the signal to produce a time series of strain-rate at virtual stations along the cable. The virtual station locations (hereafter simply termed 'stations' as the closest analog in common nomenclature) are estimated by the two-way travel-time of the pulsed light as the total length of the cable and wavespeed of the light are known. As the individual pulses of light have a finite duration, the length of the pulses are also known and this length acts as a spatial low-pass filter, termed the gauge length (e.g. Dean et al., 2017; Lindsey et al., 2020). Since particle velocity at a location for an elastic solid is equal to the product of the strain with the phase velocity of the passing wavefront (e.g. Lindsey et al., 2020; Challu et al., 2021), we can utilize DAS data with the same methods commonly used in seismological analysis, but with significantly denser sampling.

The use of nearly co-located strain-rate proportional DAS and particle velocity proportional geophones within ~2 km of an explosive source provides a chance to test the similarity between the two recording methods and to isolate short wavelength features which may not be resolvable even with a dense nodal geophone array. This is particularly relevant for the DAG phase of the experiment as the geologic setting contains small heterogeneities which lead to wavefield scattering, but at a scale which is unresolvable with 4.5-Hz geophones at 50-m spacing. In this report, we apply a battery of tests to the DAS data and, where possible, compare the results to what would be inferred from the geophone data alone. Specifically, we produce a 1D P wavespeed model based on seismic refraction, estimate the amplitude spectra of the direct arrivals, measure inter-station coherence, apply 1D beamforming and complex semblance analysis to determine wavefield slowness, and convert the strain-rate data to particle velocity. These tests find similar results for both datasets, but as the spatial sampling of the DAS is much higher than the geophones, the spatial resolution of the DAS is correspondingly higher.

2. DATA

The seismic instrumentation we focus on here is the high station density geophone array, termed the DAG Large-N array, and the DAS cable located within ~2 km of the DAG source borehole. The 482 geophones have peak sensitivity at 4.5-Hz, are sampled at 500 samples per second, and are distributed in an approximately regular grid around the borehole with two dense lines, one to the southwest and the other to the southeast (Fig. 1-1, inset). The DAS line parallels the southeastern dense line of geophones and contains 2240 individual virtual stations (with the first 40 and last 8 removed from analysis due to low signal-to-noise conditions) with a spatial spacing of 1 m and a gauge length of 2 m, recorded at 2000 samples per second. The frequency response of the (virtual) DAS stations is generally regarded to be flat through their passband and is proportional to strain-rate (e.g. Lindsey et al., 2020). A direct comparison of a record section of waveforms illustrates the substantially higher spatial resolution in the DAS data compared with the geophone data even when the DAS data is decimated to 1 in 10 waveforms (Fig. 2-1).

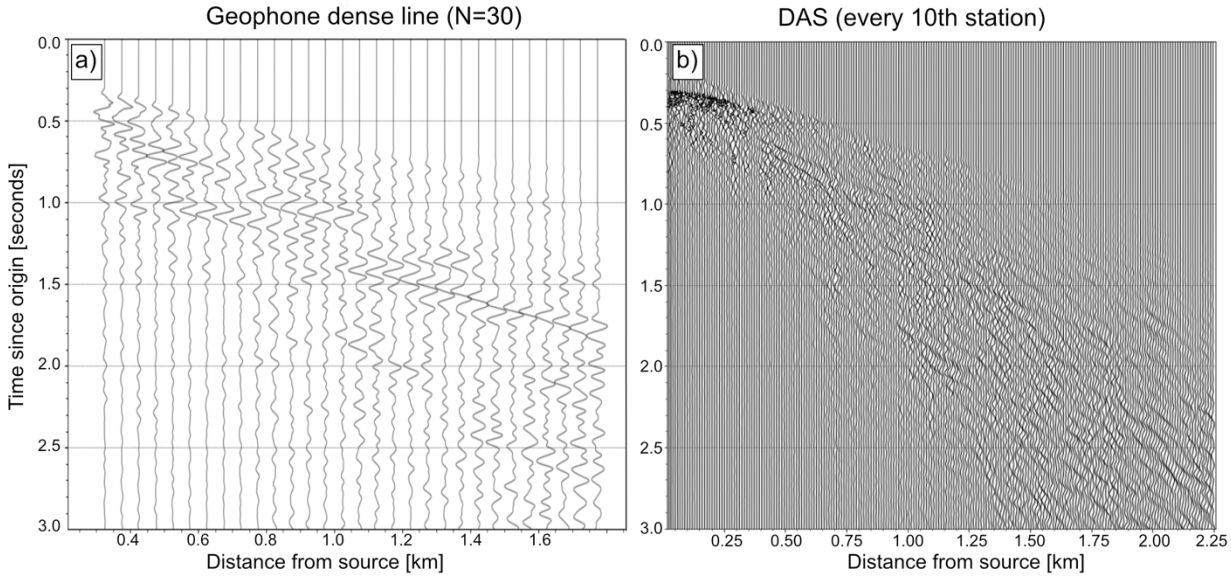

Figure 2-1: Comparison of waveforms along the dense geophone line (a) to the southeast of the source with the approximately co-located DAS data (b). Note that the waveforms for the geophones have been differentiated once to acceleration while the DAS waveforms are proportional to strain-rate. DAS data is plotted only every 10th virtual station to avoid overlapping waveforms.

The seismic source used in this study is the second of four chemical explosions detonated, termed "DAG-2", with an explosive energy of 50,000 kg TNT-equivalent. This explosion was detonated at a depth of 299 m below the ground surface and the explosion time is origin time for each trace. As can be seen from Figures 2-1 and 2-2, the magnitude of the source results in a clear signal above the background noise.

Figure 2-2 provides a view of eighteen neighboring stations within the DAS cable (i.e. ~9 gauge lengths). Qualitatively, these strain-rate waveforms (i.e. strain-rate-grams) show a high degree of similarity to each other in the characteristics of the initial arrival phase, coda, secondary arrival phase, and later scattered arrivals. Variations are generally gradational between strain-rate-grams, but there are some groups of stations where the characteristics of the seismic arrival phases and coda change sharply. The difference between the first and second groupings of strain-rate-grams is in the

initial arrival phase. The first grouping could be further subset as the top two strain-rate-grams contain a distinctive negative polarity in the coda, but these top four strain-rate-grams are grouped because their initial arrival phase starts slightly negative and then is relatively flat and positive. The second set, however, has the same initial negative motion, but this is followed by a more peaked triangular waveform. The third set reverses this change in the initial arrival phase back to the relatively flat waveform observed in the first set and the first positive cycle of the secondary arrival phase is relatively reduced in amplitude. The bottom set has the same plateau-like initial arrival phase, but a larger positive first cycle to the secondary phase than the third set. These sets of changes occur over distances of ~3-6 meters, which is significantly smaller than the sensitivity of the passing seismic waves and therefore may reflect variations in the cable or its ground-coupling rather than discernable subsurface structures.

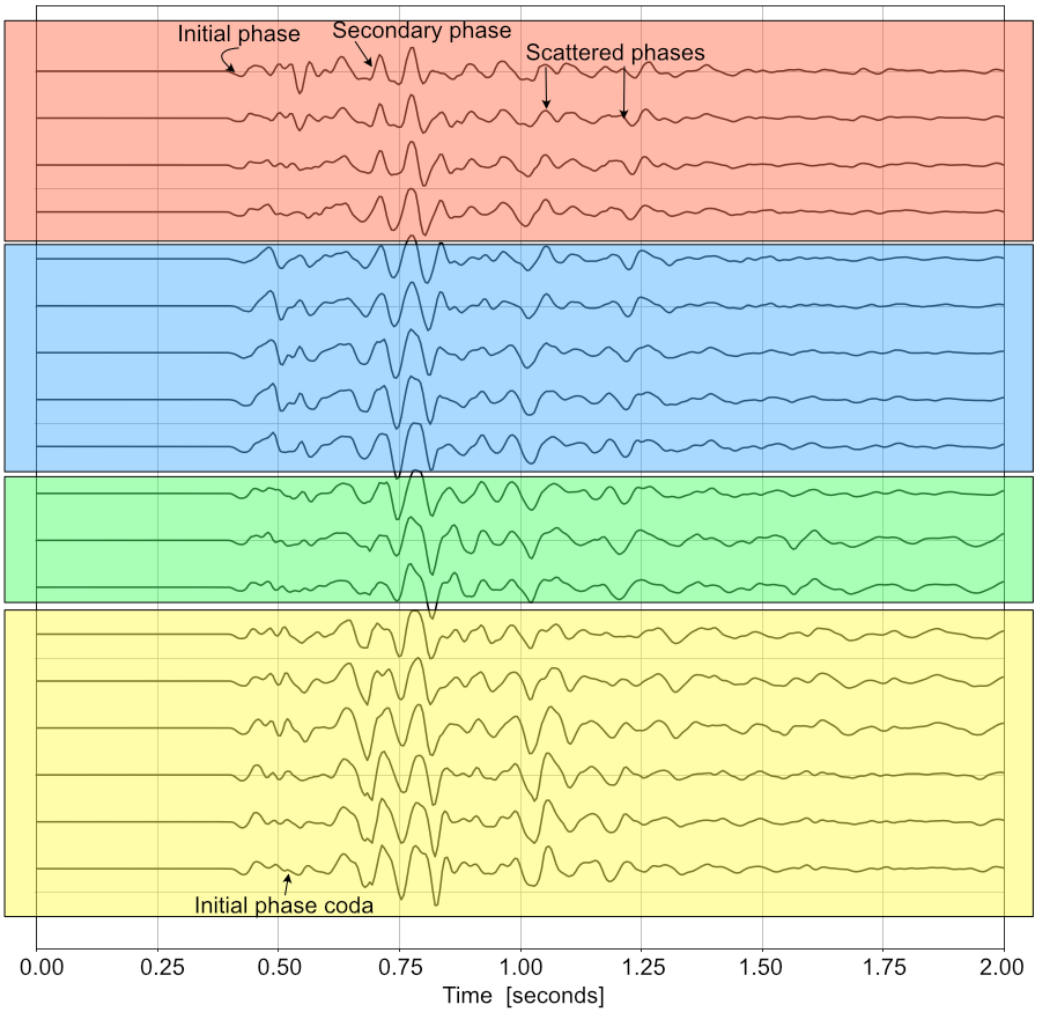

Figure 2-2: Zoom in on a subset of DAS data with initial phase, initial phase coda, secondary phase, and scattered phases labeled. Colored boxes indicate qualitatively similar waveform groups based on characteristics of initial and secondary phases. Stations are sequentially further from the source from top to bottom with a station spacing of ~1 m.

3. FIRST-ARRIVAL REFRACTION ANALYSIS

The first break arrival times, that is the earliest point in time following the source origin time in which the high frequency characteristic of the strain-rate-gram or seismogram makes a discernable change, observed on the DAS data indicate three main arrival regimes: a direct, upgoing, arrival from the 299 m depth buried source to the surface in the first ~300 m horizontal offset, a refracted arrival between 300 m and 1000 m with an apparent moveout velocity of ~2200 m/s, and a second refracted arrival at distances greater than 1000 m with an apparent moveout velocity of ~5000 m/s (Figure 3-1). Using only the geophone data (Figure 3-1, red diamonds), we can observe the two refracted arrivals, but not the direct arrival. The DAS was deployed closer to seismic ground zero (SGZ), without fear of ground motion clipping the sensor, so was able to capture arrivals that the geophones were not. Furthermore, the significantly greater number of measurements provided by the DAS indicate less variability in arrivals from the ~2200 m/s layer than from the ~5000 m/s layer. Based on observations from hand-picking the first breaks, we suggest this variability reflects the more emergent refracted arrivals from the deeper layer simply being more difficult to identify by sight.

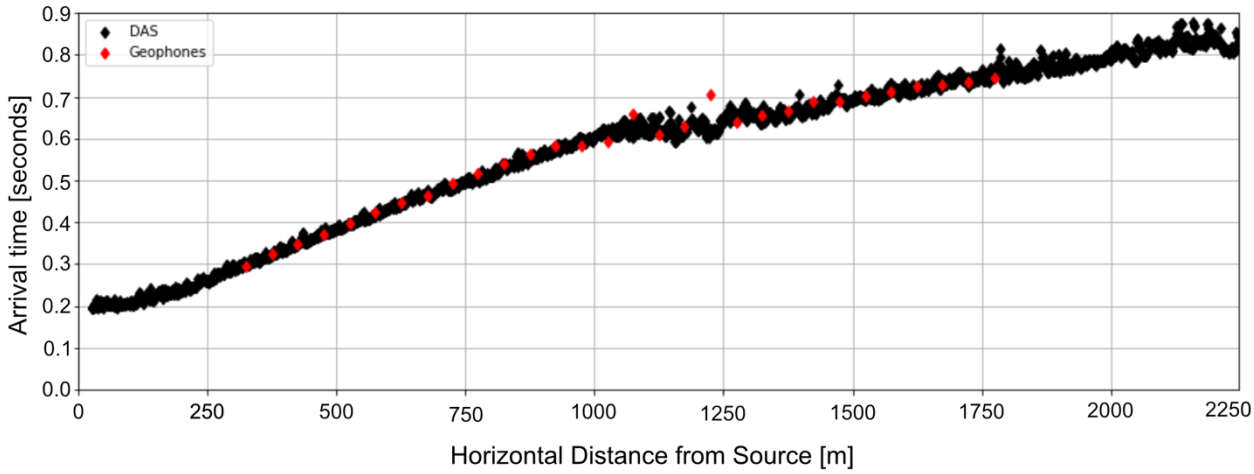

Figure 3-1: First break picks on the geophones (red) and the DAS (black). Estimating velocity from the slopes of the straight-line segments returns a first layer wavespeed of 2227 m/s and a second layer wavespeed of 4968 m/s.

We model the travel times assuming a 1D, isotropic, compressional wavespeed geometric model following standard refraction analysis modified for a buried source (Appendix A.1). To quantify the variability in this model, we apply bootstrap resampling with 1000 realizations. Each realization draws the two cross-over points from Gaussian distributions centered on the above-mentioned approximations of 300 m and 1000 m with variabilities of 10 m and 30 m respectively. We then sample arrivals randomly from the three regimes defined by the new cross-over points to model the direct arrival and two refractions and run forward modeling to estimate the wavespeed in three layers and the thickness of the top two layers. The results (Fig. 3-2) show a good visual fit to the data and clear local minima in the misfit functions for the wavespeed in the upper layer, thickness of the upper layer, and thickness of the middle layer, while the wavespeeds of the two lower layers are found directly from the slopes of the refracted arrivals. The resulting model (Fig. 3-2e and Table 3-1) is consistent with previous wavespeed models for the study area (e.g. Toney et al., 2019). Moreover, the uncertainties from the bootstrapping analysis reflect the qualitatively high

scatter in the later refracted arrivals in that the deepest layer wavespeed has the largest uncertainty (over 50 m/s).

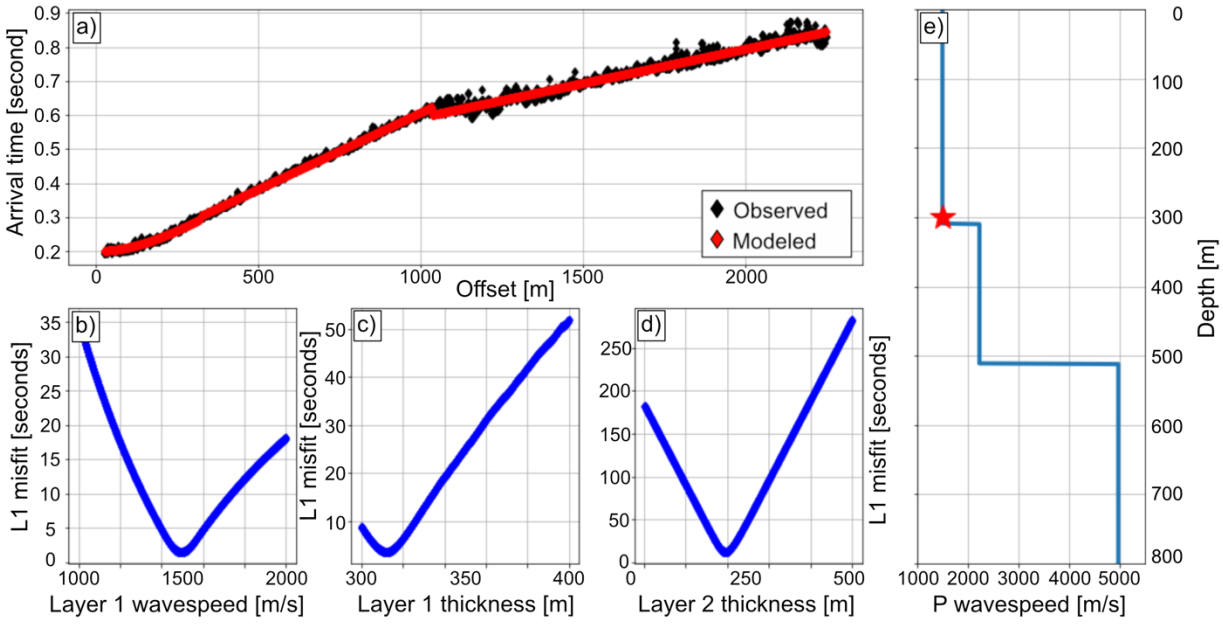

Figure 3-2: Refraction analysis of the first break picks. (a) Comparison of the observed arrival times and the predicted arrival times based on the best-fit 1D wavespeed model. (b-d) Misfit functions for the wavespeed of the upper layer, thickness of the upper layer, and thickness of the middle layer, respectively. (e) Best fit 1D wavespeed model based on refraction analysis. Red star indicates the source depth.

Table 3-1. Seismic wavespeed model determined by refraction analysis. Uncertainties reflect standard deviation in 1000 bootstrap realizations.

Layer	Thickness [m]	P Wavespeed [m/s]
1	310 +/- 1.3	1496 +/- 4.1
2	202 +/- 3.2	2227 +/- 15.6
3	N/A	4968 +/- 56.8

The analysis of seismic refraction for DAS data is a natural "first pass" method of data quality control and helps produce an initial wavespeed model. The dataset of first break picks is straightforward to determine but can be time-intensive to produce. Nonetheless, first break picks are useful for understanding the seismic phases contained in the data and producing time windows appropriate for further analysis. Moreover, DAS has been shown to have the same phase-response as broadband velocity instruments at frequencies less than ~1 Hz (e.g. Lindsey et al., 2020) and the high data density provides greater confidence in the observations than could be achieved with geophones alone.

4. AMPLITUDE SPECTRA

We isolate the frequency content of the initial arrival phase by first computing the Continuous Wavelet Transform (CWT; Mallat, 1999) with a complex Morlet mother wavelet. The CWT is defined for an arbitrary time series s(t) as:

$$S_{\omega}(a,\tau) = \frac{1}{|a|^{\frac{1}{2}}} \int_{-\infty}^{\infty} s(t)\overline{\psi}\left(\frac{t-\tau}{a}\right)dt \ \#(1)$$

where $\overline{\psi}$ is the complex conjugate of the wavelet function, τ is the wavelet time, and a is the scale, which for the Morlet wavelet, is inversely proportional to frequency, and ω is the control parameter for the wavelet function (see Appendix A.2 for details of the Morlet wavelet). We then extract a time window from 0.1 seconds before the arrival to 0.3 seconds after the arrival. The amplitude spectra is defined as:

$$P_{ss}(a) = \sum_{\tau} S_{\omega}(a,\tau) * \overline{S_{\omega}}(a,\tau) \ \#(2)$$

where τ is the arrival time window and $\overline{S_{\omega}}(a,\tau)$ is the complex conjugate of the CWT. Figure 4-1 presents the spectra along the data line after converting scale to frequency and normalizing at each station. This indicates that the peak in the amplitude spectra for the initial arrival is approximately 10 Hz as observed in both the geophone and DAS data. However, there are substantial variations around this median value. While it might be unclear how well resolved these variations are in the geophone data, the same general patterns are observed in the DAS data. Notably, there is an offset in the peak around 800 m from the source. At 1000 m there is both an upper peak at slightly above 10 Hz and a lower peak at ~5 Hz, and a low frequency peak at 1750 m at about 4 Hz. At all distances, the signal appears confined between ~3 Hz and ~20 Hz and we therefore restrict the following analysis to that frequency band.

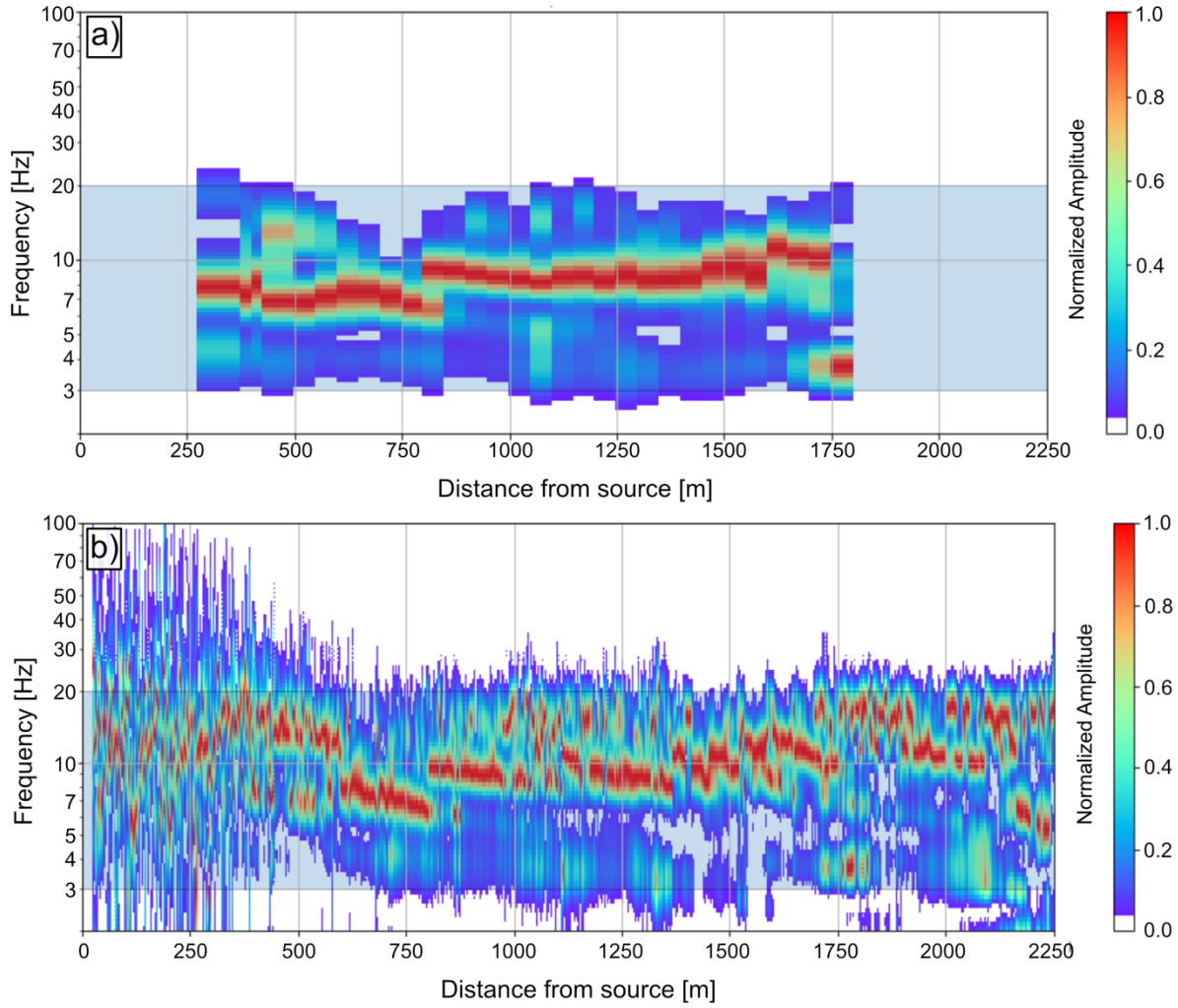

Figure 4-1: Normalized amplitude spectra along the dense line for the initial arrival phase based on the (a) geophone data and (b) DAS data. The time window for the initial arrival phase is determined as the pick time minus 0.1 seconds to the pick time plus 0.3 seconds. Note that the vertical axis is logarithmic.

5. WAVELET COHERENCY

We quantify the similarity between two waveforms with wavelet coherency defined as:

$$C_{sr}(a) = \sum_{\tau} S_{\omega}(a,\tau) * \overline{R_{\omega}}(a,\tau) \#(3)$$

$$Coh(a) = \frac{C_{sr}(a)^2}{P_{ss}(a) * P_{rr}(a)} \#(4)$$

where $C_{sr}(a)$ is the cross-spectra between wavelet transforms of two waveforms, s(t) and r(t), τ is the initial phase arrival time window, and Coh(a) is the normalized cross-spectra. From our dataset of inter-station wavelet coherencies for each pair of stations along the DAS cable, we illustrate the result of wavelet coherency with respect to inter-station distance both statistically in the form of Probability Density Functions (PDFs; Figs. 5-1, 5-2) and qualitatively by looking at peak wavelet coherency for a set of central stations along the line (Fig. 5-3).

The geophone particle velocity and DAS strain-rate data show similar shapes in wavelet coherency as a function of inter-station distance, but the DAS data is significantly more densely sampled leading to smooth distributions (Fig. 5-1). The PDFs of the geophone coherency appear saturated because the distance-coherency space is poorly sampled resulting in relative probability with few measurement instances. At the low frequency end, 3 Hz, the wavelet coherency tends towards the maximum value of 1.0 with much of the probability space above 0.6. At higher frequencies, the distributions are broader with less high probability at high wavelet coherency. While these patterns are consistent in both the geophone and DAS data, the geophone data appears more scattered and therefore little inference can be made based on these data. The DAS data, however, is more able to explore the probability space due to the dense station coverage.

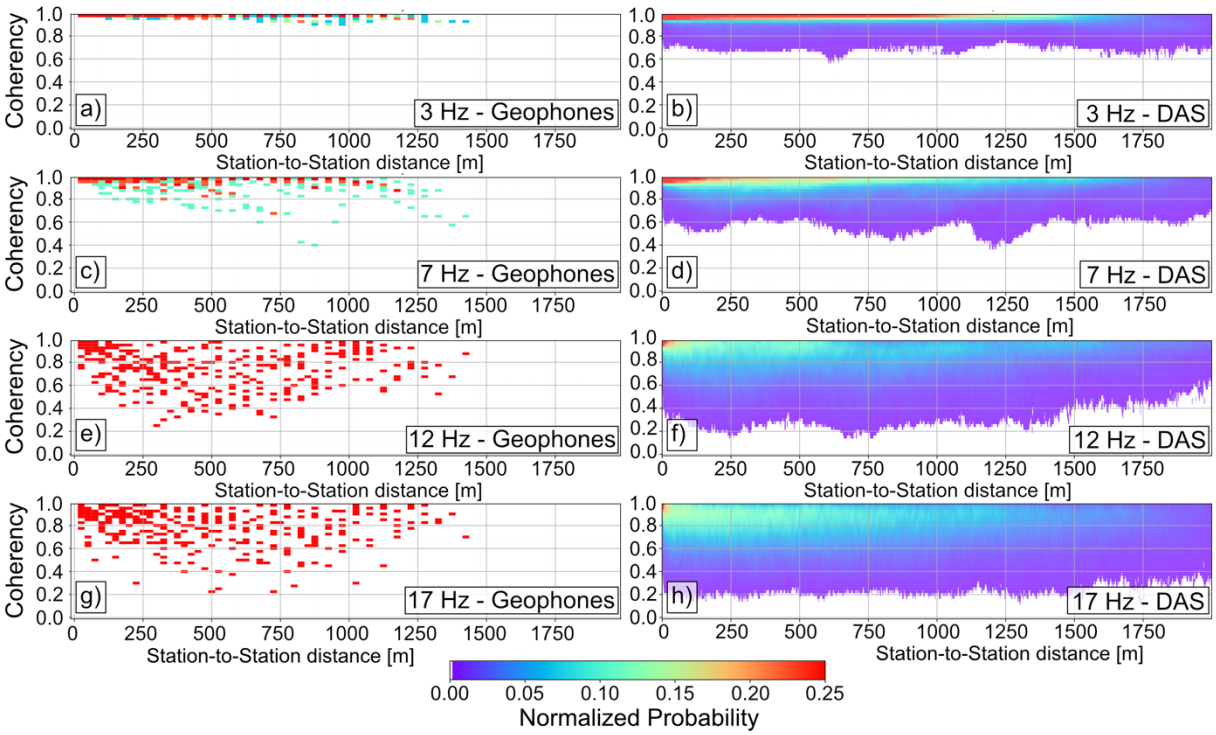

Figure 5-1: Probability density functions of initial arrival phase wavelet coherency vs. inter-station distance on the geophones (a, c, e, g) and DAS (b, d, f, h) for 3 Hz to 17 Hz as indicated within each panel. Time window for the initial arrival phase is determined as the pick time minus 0.1 seconds to the pick time plus 0.3 seconds.

The high spatial sampling of the DAS data is also apparent when comparing the mean wavelet coherency (Fig. 5-2). At 3 Hz and 7 Hz, the mean wavelet coherency is flat at the maximum coherency in the PDFs, which is 0.975, for most inter-station distances. These high mean values roll off at different distances for the geophone and DAS data and different frequencies. However, at higher frequencies, the means from the geophone data are significantly lower with larger scatter than the means and variability from the DAS data. While these high frequency values show lower wavelet coherency than the low frequency, the means for the DAS data still show values of ~0.9 for most inter-station distances, indicating a high level of similarity for the initial arrival.

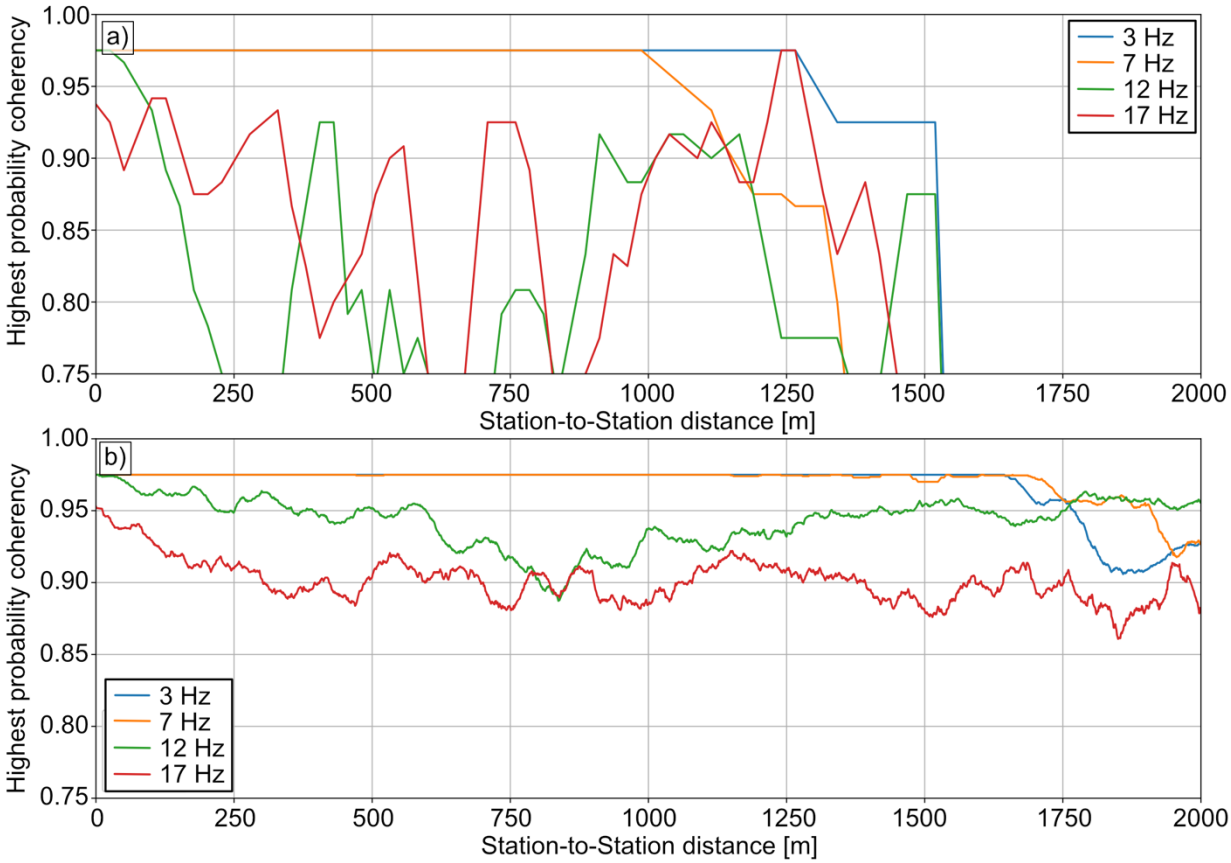

Figure 5-2: Mean wavelet coherency vs. distance for a subset of frequencies extracted from the probability density functions in Figure 5-1 for geophones (a) and DAS (b).

The coherency PDFs are dependent on distance between pairs of recording stations rather than distance from the seismic source. As longer paths between the source and receiver can accumulate more scattered seismic energy, we expect generally lower coherency at longer offsets. We evaluate this by considering coherency as a function of inter-station distance for a set of reference stations and plot cases where the reference station is farther from the source than the second station as negative distances (Fig. 5-3). These measurements have significant scatter and therefore we present versions that have been smoothed with Gaussian filters to highlight patterns. However, we do not observe many clear trends in these data. As with the PDFs, we generally see that lower frequency measurements have higher coherency. Comparing the trends between the geophone coherency and the DAS coherency, we observe a qualitative similarity at 3 Hz and 7 Hz, but with more short-wavelength variations in the DAS coherency. The differences in coherency at higher frequencies may be a function of the geophone response, short-wavelength scattering, or reduced source energy above 10 Hz.

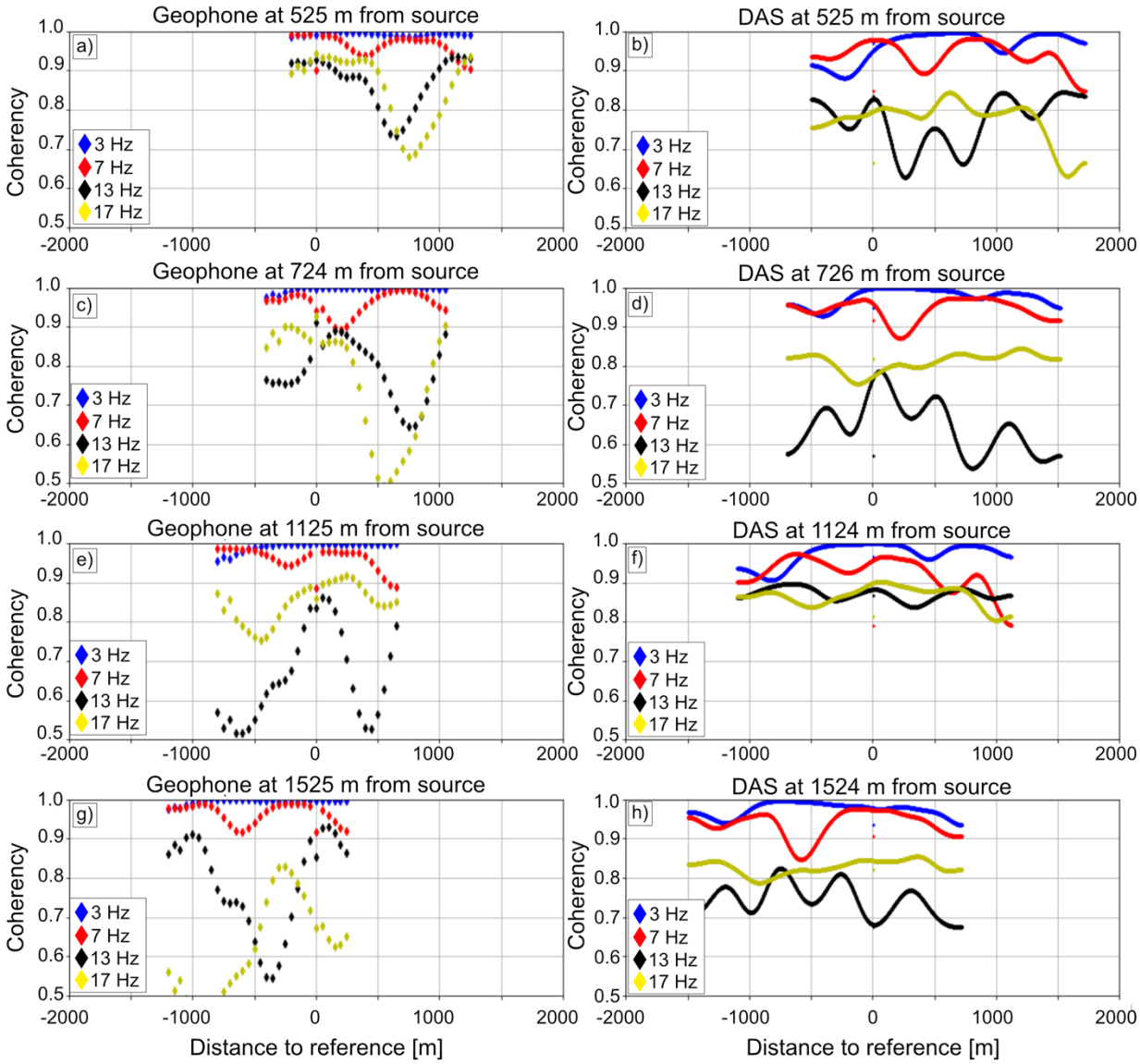

Figure 5-3: Wavelet coherency vs. inter-station distance for a set of central stations (rows) and frequencies (colors) for geophones (a, c, e, g) and DAS (b, d, f, h). Distance is the difference between the reference station and the second DAS or geophone. Negative values indicate the second station is nearer to the source than the reference. Functions have been smoothed with a Gaussian filter with a sigma of 100 m.

6. PHASE VELOCITY

The relationship between particle velocity, $\dot{u}(t)$, and strain, $\varepsilon(t)$, for DAS data is proportional to the phase velocity, $c(t)$, of the seismic wavefield (e.g. Lindsey et al., 2020; Lior et al., 2021).

$$\dot{u}(t) = c(t) * \varepsilon(t) \#(5)$$

For the case of a single plane wave traveling across an array, using a constant wavespeed may be adequate, but a more accurate approximation can be derived by considering the time-dependent phase velocity. Here we apply two independent methods of estimating the instantaneous phase velocity: 1) beamforming (e.g. Rost and Thomas, 2002) of short, overlapping time windows and 2) complex semblance (Shi and Huo, 2019; Lior et al., 2021). These quantities are defined as:

$$Beam\ Power(t,p_{radial}) = \sum_{N} s(t + p_{radial} * dr) \ \#(6)$$

$$Sem(t, p_{radial}) = \frac{1}{N}\left(\frac{\sum_N s(t + p_{radial} * dr)^2 + \sum_N H(s(t + p_{radial} * dr))^2}{\sum_N [s(t + p_{radial} * dr)^2 + H(s(t + p_{radial} * dr))^2]}\right) \#(7)\#\#\#$$

for waveform $s(t)$, time t, radial direction slowness (reciprocal of phase velocity) p_{radial}, distance between station and reference point dr, number of stations in the stack N, and Hilbert transform $H(s(t))$. Both algorithms are applied on both the geophone data and the DAS data filtered between 3 and 20 Hz with a zero-phase filter. The beamforming results are similar between the geophone and DAS data (Fig. 6-1), but with some significant differences. However, semblance results are significantly different between the two datasets (Fig. 6-2).

The 1D beamforming results appear atypical compared with more common beamforming analyses because the back-azimuth, the angle pointing from the station towards the source, is a known constant value as the array is arranged radially outward from the source whereas other studies work in 2D array processing to estimate back-azimuth and slowness (e.g. van den Ende and Ampuero, 2021 and references therein). Nonetheless, the 1D beamforming results (Fig. 6-1) show beam power maxima at slowness values of ~0.5 – 1 s/km within ~1 second after the initial P wave arrival. For the DAS beamforming results, most of the beam power is in the positive slowness space following the initial arrival, whereas the geophone results have significant negative slowness in the early times. As this slowness is in the radial direction, the positive values indicate forward propagating waves whereas negative slowness indicates back-scattered energy. Back-scattered energy cannot arrive before the initial arrival by definition and therefore this apparent back-scattered energy on the geophone data is an artifact. As the DAS data contains less of this artifact, we can infer that the DAS provides an improved estimate of the wavefield slowness. Additionally, the array response functions (Appendix A.3) show diagonal artifacts from the synthetic source and these artifacts are more pronounced with the geophone data than with the DAS data.

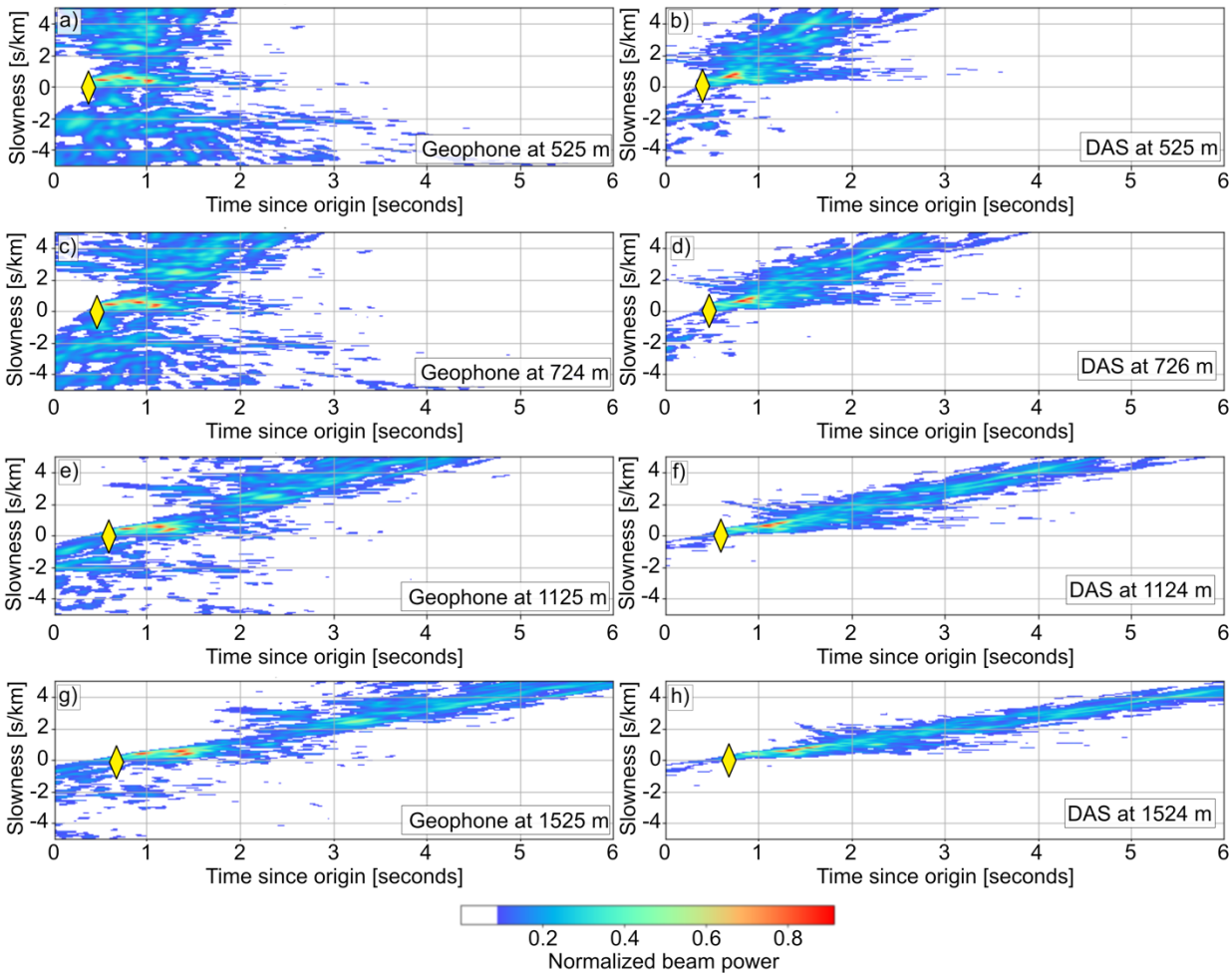

Figure 6-1: Beam power results at a subset of geophones and nearest DAS stations. Bottom right of each panel gives the horizontal distance from the source borehole to the reference receiver. Yellow diamond at 0 [s/km] slowness and ~0.4 - 0.7 seconds indicates the picked arrival time. Local maxima in the beam power suggest coherent energy passing through the reference station at the x-axis time and y-axis radial direction slowness.

The semblance results with the DAS data show local maxima between 0 and 1 s/km slowness for most of the time-series whereas the geophones show non-zero semblance throughout the time-slowness space (Fig. 6-2) From the geophone data, there is a slight local maximum semblance at ~0.5 s/km, but this maximum is only slightly higher semblance than the background. However, with the DAS data there is a distinct trend of peak semblance at 0.5 – 1.0 s/km at most points in time with isolated maxima at -1.0 – (-0.5) s/km later than ~6 seconds, indicating late back-scattered arrivals. Repeating this semblance calculation following the CWT of the data for scales between 3 Hz and 20 Hz found little change with frequency for the phase velocity over time. This suggests the scattered, converted waves travel with the same wavespeed as shallow layers and this includes both forward and backward scattering. Moreover, the semblance images present a more continuous function of phase velocity with time than the beamforming, and we therefore use the semblance derived phase velocity for converting the DAS strain-rate data into ground velocity.

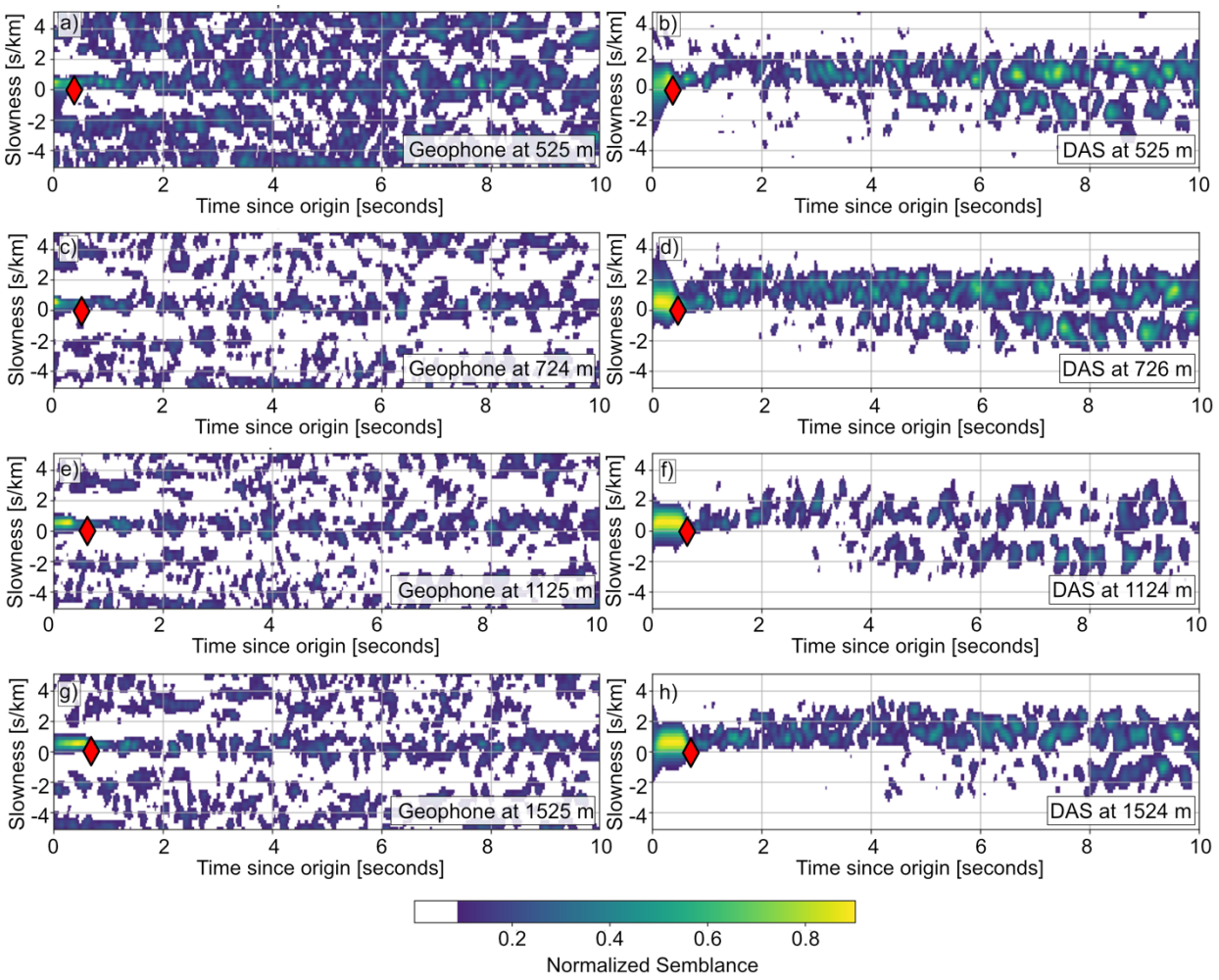

Figure 6-2: Semblance results at a subset of geophones and the nearest DAS stations. Lower right label in each panel indicates distance of reference station from the source. Red diamond at 0 [s/km] slowness indicates the manually picked arrival time.

7. CONVERSION OF STRAIN-RATE TO PARTICLE VELOCITY

The DAS strain-rate data can be compared with the geophone particle velocity data recorded at the geophones after integrating with respect to time and scaling by the phase velocity (Equation 5). Following Lior et al. (2021), we extract phase velocity at each DAS station location as a function of time from the peaks in the smoothed semblance plots.

$$c(t) = \frac{1}{p_{radial}(\max\,(Sem(t)) + \epsilon} \#(8)$$

Here ϵ is a waterlevel term to avoid division by 0 and $p_{radial}(\max\,(Sem(t))$ refers to the radial direction vector slowness at the local maximum value of the semblance at time t. After applying Equation 5, we then slant stack the DAS-inferred particle velocity waveforms at the geophone locations for a direct comparison with the radial component seismograms (Fig. 7-1). Slant stacking in the wavelet domain is defined as:

$$\dot{U}_{das}(a, \tau, x) = \frac{1}{N}\sum_{N} \dot{U}_{das}(a, \tau + \overline{p}_{radial} * dr) \#(9)$$

where $\overline{p}_{radial}$ is 1 s/km, representing the approximate mean slowness observed in the semblance plots, x is the location of the geophone, and dr is the distance from the geophone to the DAS station. Following stacking, the inverse wavelet transform is used to return the signal to the time domain. Qualitatively, these waveforms appear similar, but correlation coefficients range from –0.12 to 0.75 with a mean value of 0.40 (or 0.49 if focused only on the initial arrival). A point where the misfit can be visually assessed is an apparent shift in the initial arrival phase at seismograms within ~1000 m offset. There are also various points where secondary arrivals are lost in the stacked DAS based ground motion (i.e. the waveforms at ~425 m offset, at ~1 second) or shifted (i.e. waveforms at ~1350 m, at 1.5 seconds). These shifts may be due to non-optimized slowness corrections applied in the stacking as our algorithm uses only a single constant slowness correction or the misfits may be due to the geophones being deployed ~20 m away from the DAS line. Development of an optimized correction may provide new insights into the subsurface structure, but that is outside of the scope of this study.

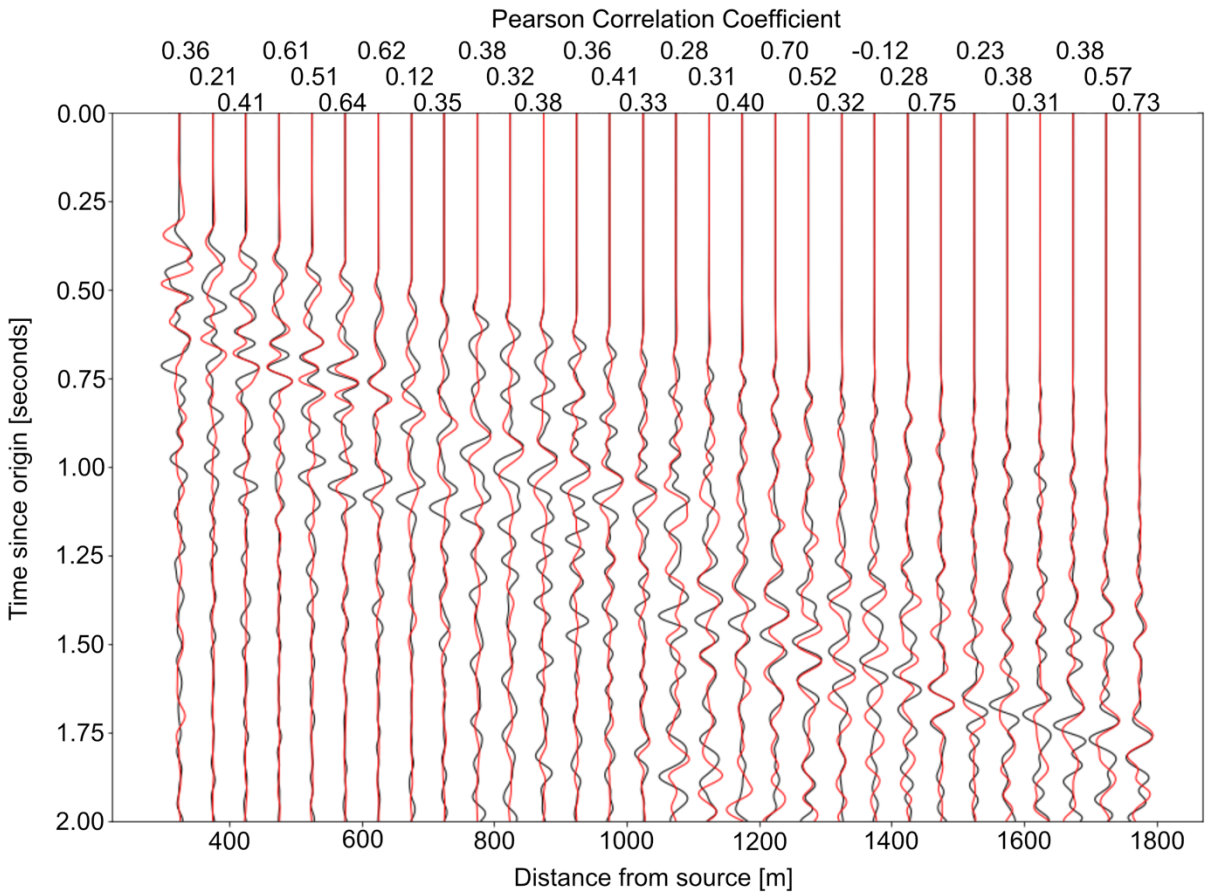

Figure 7-1: Comparison between geophone-based particle velocity (black) and DAS-based particle velocity (red) at geophone locations. Cross-correlation coefficient between the waveforms indicated at the top of each waveform pair. Mean correlation coefficient is 0.40 for the 2 second time window. All waveforms have been normalized for presentation.

We can also consider waveform similarity as a function of frequency, rather than time. Figure 7-2 uses the CWT to measure the cross-correlation for each scale between the geophone and DAS particle velocity. This shows positive correlations at frequencies above ~5 Hz. These correlation values likely are due to the reduced response of the geophones at frequencies less than ~4 Hz and Figure 4-1 which indicates much of the signal is focused near 10 Hz. The high correlation between ~6 Hz and ~15 Hz for most source-receiver offsets further supports the interpretation that the source signal is primarily exciting energy at ~10 Hz and this source signal has a larger effect on the recorded waveforms than the instrument response uncertainties.

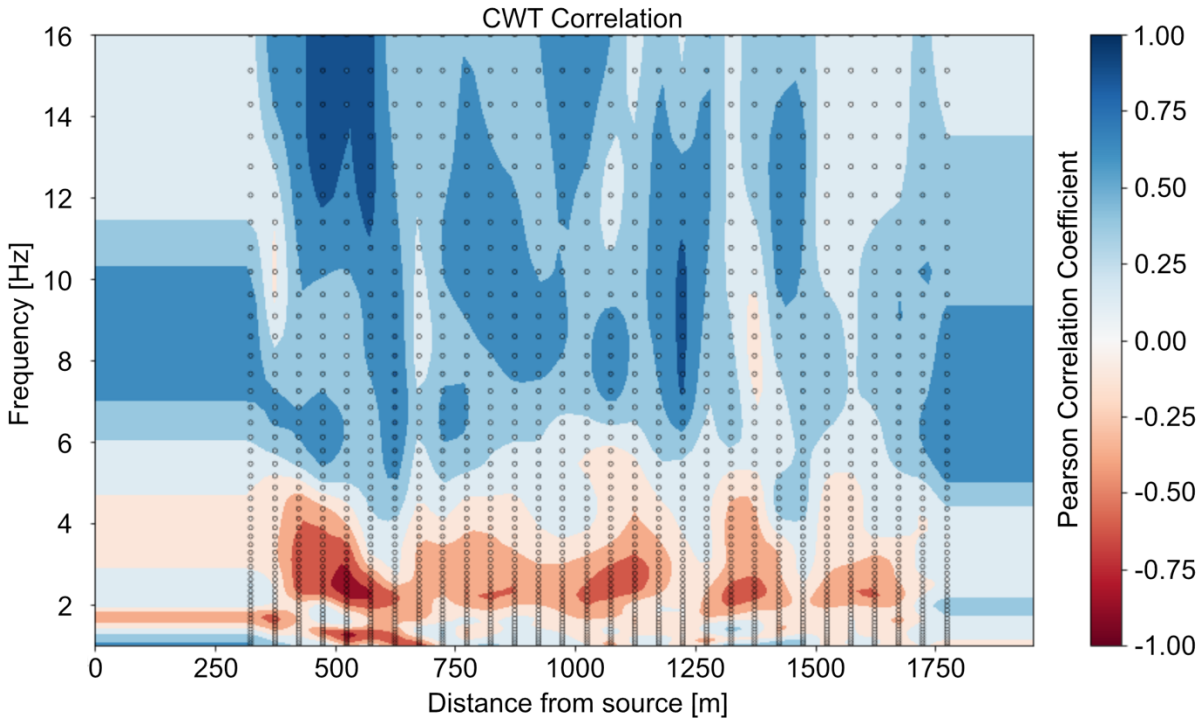

Figure 7-2: Wavelet domain cross-correlation between geophone-based particle velocity and DAS-based particle velocity as a function of distance from the source and frequency. Measurement points are plotted as colored dots and the background is the contoured version of those points. Frequency is the reciprocal of the Morlet wavelet scale.

8. CONCLUSIONS

The data observed on the DAS from the DAG-2 explosion provides a substantially higher spatial resolution of the seismic wavefield than the data obtained by a traditional geophone array. The primary take-aways from our battery of tests are:

- Refraction analysis with bootstrap resampling of arrivals observed on DAS stations found a 1D wavespeed model consistent with previously published models and provides uncertainties.
- Amplitude spectra from DAS and geophone data show maximum values near 10 Hz and significant values between 3 and 20 Hz.
- Secondary trends in amplitude spectra are consistent between the two datasets, but the DAS data provide increased detail over the geophone data.
- Coherency values tend to show higher values at lower frequencies and shorter inter-station offsets.
- The DAS data provides a significantly denser probability function of coherency due to the high spatial sampling density.
- Both beamforming and semblance provide estimates of time-dependent phase velocity, but semblance on the DAS data provide a more continuous function than alternative approaches, which is useful in converting strain-rate to velocity.
- Wavelet domain slant stacking of particle velocity at DAS stations onto geophone locations provides a high level of similarity to geophone recorded particle velocity.

These analyses show that DAS data can provide improved wavefield characterization relative to the dense line of nodal geophones for DAG-2. Furthermore, the geophone data could be reproduced from the DAS data alone if geophones were unavailable. Current shortcomings of the DAS data include that the array geometry is linear and strain-rate data is recorded in the radial component of the cable. However, these weaknesses can be overcome through creative tests of cable arrays and development of engineered, helically wound, fiber-optic cable.

REFERENCES

[1] Challu, C., Poppeliers, C., Punoševac, P., and Dubrawski, A. (2021). Explosion Discrimination Using Seismic Gradiometry and Spectral Filtering of Data. *Bulletin of the Seismological Society of America*, 111 (3): 1365-1377, doi: 10.1785/0120200304

[2] Darrh, A., Poppeliers, C., and Preston, L. (2019). Azimuthally Dependent Seismic-Wave Coherence at the Source Physics Experiment Large-N Array. *Bulletin of the Seismological Society of America*, 109 (5): 1935-1947, doi: 10.1785/0120180296

[3] Dean, T., Cuny, T., and Hartog, A. H. (2017). The effect of gauge length on axially incident P-waves measured using fibre optic distributed vibration sensing. *Geophysical Prospecting*, 65 (1): 184-193, doi: 10.1111/1365-2478.12419

[4] van den Ende, M. P. A. and Ampuero, J.-P. (2021). Evaluating seismic beamforming capabilities of distributed acoustic sensing arrays. *Solid Earth*, 12, 915-934, doi:10.5194/se-12-915-2021

[5] Lindsey, N. J., Rademacher, H., and Ajo-Franklin, J. B. (2020). On the Broadband Instrument Response of Fiber-Optic DAS Arrays. *Journal of Geophysical Research – Solid Earth*, 125 (2), doi:10.1029/2019JB018145

[6] Lior, I., Sladen, A., Mercerat, D., Ampuero, J.-P., Rivet, D., and Sambolian, S. (2021). Strain to Ground Motion Conversion of DAS Data for Earthquake Magnitude and Stress Drop Determination. *Solid Earth*, doi:10.5194/se-2020-219

[7] Mallat, S. (1999). A wavelet tour of signal processing. Elsevier.

[8] Rost, S. and Thomas, C. (2002). Array Seismology: Methods and Applications. *Reviews of Geophysics*, 40 (3) 1008, doi:10.1029/2000RG000100

[9] Shi, T. and Huo, S. (2019). Complex Semblance and Its Application. *Journal of Earth Science*, 30: 849-852, doi:10.1007/s12583-018-0829-x

[10] Toney, L. D., Abbot, R. E., Preston, L. A., Tang, D. G., Finlay, T., and Phillips-Alonge, K. (2019). Joint Body- and Surface-Wave Tomography of Yucca Flat, Nevada, Using a Novel Seismic Source. *Bulletin of the Seismological Society of America*, 109 (5): 1922-1934, doi:10.1785/0120180322

[11] Zhan, Z. (2020). Distributed Acoustic Sensing Turns Fiber-Optic Cables into Sensitive Seismic Antennas. *Seismological Research Letters*, 91 (1): 1-15, doi:10.1785/0220190112

APPENDIX A.

A.1. Refraction Modeling

The seismic refraction analysis uses forward modeling with standard formulae altered to account for the source depth.

Table A-1: Parameters used in refraction modeling.

Parameter	Description
z	Source depth (m).
x	Horizontal offset between source and receiver (m).
h	Layer thickness (m). Subscript 1-2 indicates layer. i.e. h_1 is thickness of the top layer and h_2 is thickness in the middle layer.
v	Seismic wavespeed (m/s). Subscript 1-3 indicates layer. i.e. v_1 is wavespeed in the top layer, v_2 is wavespeed in the middle layer, and v_3 is wavespeed in the lower layer.
τ	Arrival time at station (seconds).
T	Travel time in a portion of the ray-path (seconds).
i_c	Critical angle at an interface (degrees). Sub-subscripts indicate layer below the interface.

***Direct Arrival*:**
This is for stations within ~300 m horizontal offset from the source. This equation is for a one-way travel time from the buried source to the surface station.

$$\tau_i = \frac{\sqrt{z^2 + x^2}}{v_1} \#(A1)$$

***First Refraction*:**

$$v_2 = \frac{dx_i}{d\tau_i} \#(A2)$$

For stations, i, in which the first break is a refraction off the top of layer 2.

$$i_c = \sin^{-1}\frac{v_1}{v_2} \#(A3)$$

$$T_1 = \frac{\sqrt{(h_1 - z)^2 + [(h_1 - z)\tan(i_c)]^2}}{v_0} \#(A4)$$

$$T_2 = \frac{x - [(h_1 - z)\tan(i_c) + h_1\tan(i_c)]}{v_2} \#(A5)$$

$$T_3 = \frac{\sqrt{{h_1}^2 + \left[h_1\tan(i_c)\right]^2}}{v_1} \#(A6)$$

Where T_1 is the leg from the source to the top of layer 2, T_2 is the leg along the top of the interface, and T_3 is the leg from the interface to the surface.

$$\tau_i = T_1 + T_2 + T_3 \#(A7)$$

***Second Refraction*:**

$$v_3 = \frac{dx_i}{d\tau_i} \#(A8)$$

For stations, i, in which the first break is a refraction off the top of layer 3.

$$i_{c_2} = \sin^{-1}\frac{v_1}{v_2} \#(A9)$$

$$i_{c_3} = \sin^{-1}\frac{v_2}{v_3} \#(A10)$$

$$T_1 = \frac{\sqrt{(h_1 - z)^2 + \left[(h_1 - z)\tan(i_{c_2})\right]^2}}{v_1} \#(A11)$$

$$T_2 = \frac{\sqrt{{h_2}^2 + [h_2 \tan(i_{c_3})]^2}}{v_2} \#(A12)$$

$$T_3 = \frac{x - \left[(h_1 - z)\tan(i_{c_1}) + 2\,h_2\tan(i_{c_3}) + h_0\tan(i_{c_2})\right]}{v_3} \#(A13)$$

$$T_4 = \frac{\sqrt{{h_2}^2 + \left[h_2 \tan(i_{c_3})\right]^2}}{v_2} \#(A14)$$

$$T_5 = \frac{\sqrt{{h_1}^2 + [h_1 \tan(i_{c_2})]^2}}{v_1} \#(A15)$$

$$\tau_i = T_1 + T_2 + T_3 + T_4 + T_5 \#(A16)$$

To solve these equations, we first fit a linear best fit function to derive the velocities $v_2$and v_3. Then we use grid searches to solve for v_1, h_1 and h_2.

A.2. Morlet Wavelet

The wavelet domain processing uses the Morlet mother wavelet throughout because its scale term is inversely proportional to frequency. This wavelet is defined in the time domain as:

$$\psi_\sigma(t) = c_\sigma \pi^{-\frac{1}{4}} e^{-\frac{1}{2}t^2}(e^{i\sigma t} - \kappa_\sigma) \#(A17)$$

and in the frequency domain as:

$$\psi_\sigma(\omega) = c_\sigma \pi^{-\frac{1}{4}} e^{-\frac{1}{2}(\sigma-\omega)^2} - \kappa_\sigma e^{-\frac{\omega^2}{2}} \#(A18)$$

Parameters are defined as:

$$\sigma = 2\pi \#(A19)$$

$$c_\sigma = \left(1 + e^{-\sigma^2} - 2\,e^{-\frac{3}{4}\sigma^2}\right)^{-1/2} \#(A20)$$

$$\kappa_\sigma = e^{-\frac{\sigma^2}{2}} \#(A21)$$

A.3. Beamforming Array Response

The array response for beamforming is produced by propagating a pulse with a high frequency ricker wavelet through the array geometry with a slowness value of 0. The examples shown in the Figure A-1 illustrate that the array response contains a primary peak at the central time

and 0 slowness as input, but diagonal artifacts are generated because the array is linear in the radial direction.

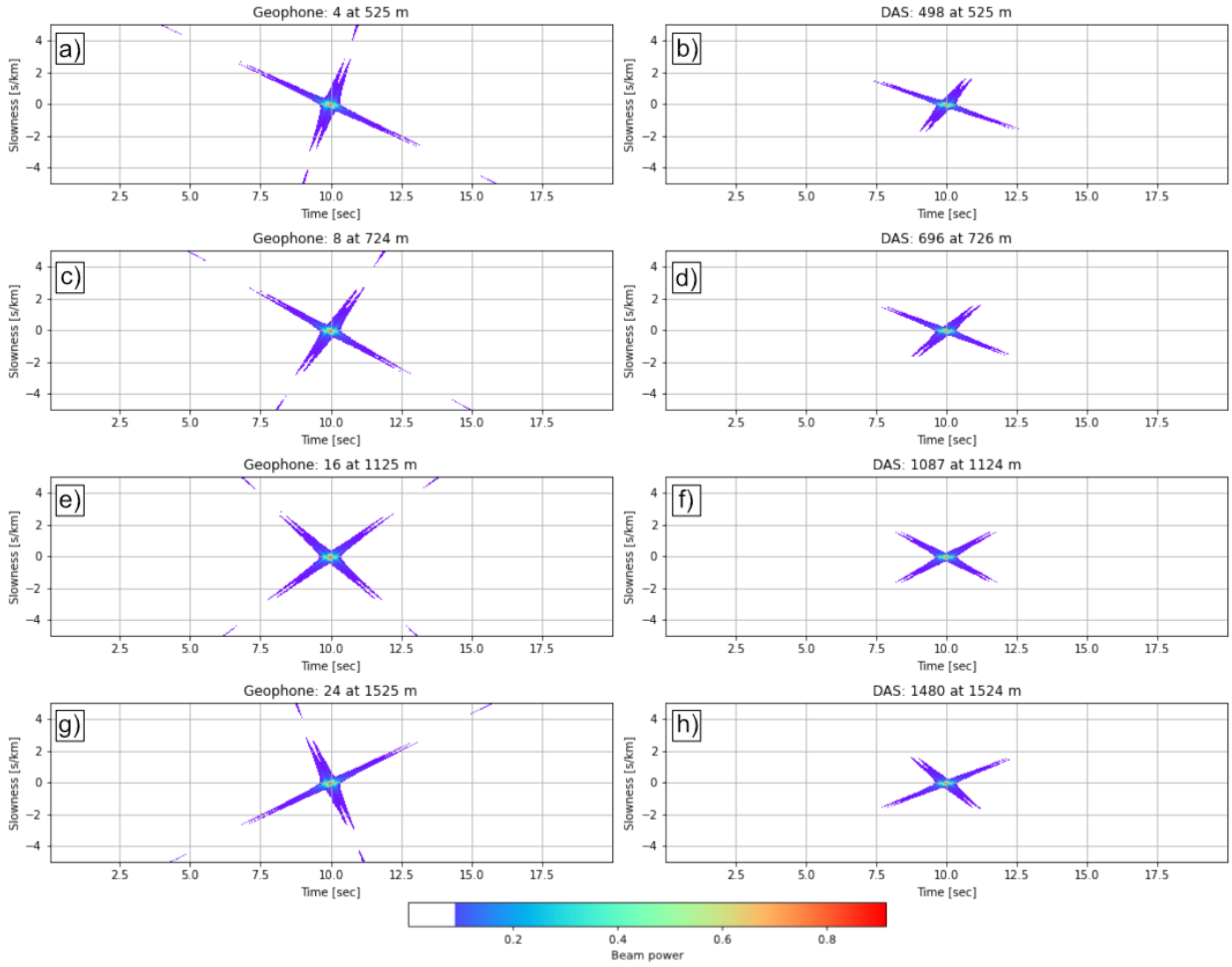

Figure A-1: Geophone (a, c, e, g) and DAS (b, d, f, h) array response for a slowness of 0 and ricker wavelet.

This page left blank

DISTRIBUTION

Email—Internal

Name	Org.	Sandia Email Address
Robert Porritt	06756	rwporri@sandia.gov
Robert Abbott	08911	reabbot@sandia.gov
Christian Poppeliers	08911	cpoppel@sandia.gov
Christian Stanciu	08911	astanci@sandia.gov
Technical Library	01977	sanddocs@sandia.gov

Email—External [redacted]

Name	Company Email Address	Company Name

This page left blank

This page left blank

Sandia National Laboratories

Sandia National Laboratories is a multimission laboratory managed and operated by National Technology & Engineering Solutions of Sandia LLC, a wholly owned subsidiary of Honeywell International Inc. for the U.S. Department of Energy's National Nuclear Security Administration under contract DE-NA0003525.